Adv. Mater. **2019**, 1900871

DOI: 10.1002/adma.201900871

Addition of the Lewis Acid $Zn(C_6F_5)_2$ Enables Organic Transistors with a Maximum Hole Mobility in Excess of 20 cm^2/Vs

Alexandra F. Paterson, Leonidas Tsetseris, Ruipeng Li, Aniruddha Basu, Hendrik Faber, Abdul-Hamid Emwas, Julianna Panidi, Zhuping Fei, Muhammad R. Niazi, Dalaver H. Anjum, Martin Heeney, Thomas D. Anthopoulos**

Dr. A. F. Paterson, Dr. H. Faber Dr. A. Basu, Dr. M. R. Niazi, and Prof. T. D. Anthopoulos
Division of Physical Sciences and Engineering
King Abdullah University of Science and Technology
Thuwal 23955-6900, Saudi Arabia
E-mail: thomas.anthopoulos@kaust.edu.sa
E-mail: alexandra.paterson@kaust.edu.sa

Prof. L. Tsetseris
Department of Physics
National Technical University of Athens
Athens GR-15780, Greece

Dr. R. Li
Brookhaven National Lab
Upton, New York, United States of America

Dr. A.-H. Emwas, Dr. D. H. Anjum
Core Labs
King Abdullah University of Science and Technology
Thuwal 23955-6900, Saudi Arabia

J. Panidi, Dr. Z. Fei, Prof. M. Heeney
Department of Chemistry and Centre for Plastic Electronics
Imperial College London
South Kensington, London SW7 2AZ, UK

Keywords: organic thin-film transistors; carrier mobility; Lewis acid; molecular doping; organic semiconductors.

Abstract

Incorporating the molecular organic Lewis acid tris(pentafluorophenyl)borane [$B(C_6F_5)_3$] into organic semiconductors has shown remarkable promise in recent years for controlling the operating characteristics and performance of various opto/electronic devices, including, light-emitting diodes, solar cells and thin-film transistors (OTFTs). Despite the demonstrated potential, however, to-date most of the work has been limited to $B(C_6F_5)_3$ with the latter serving as the prototypical air-stable molecular Lewis acid system. Here we report the use of bis(pentafluorophenyl)zinc [$Zn(C_6F_5)_2$] as an alternative Lewis acid additive in high hole mobility OTFTs based on small-molecule:polymer blends comprised of 2,7-dioctyl[1]benzothieno [3,2-b][1]benzothiophene (C_8-BTBT) and indacenodithiophene-benzothiadiazole (C_{16}IDT-BT). Systematic analysis of the materials and device characteristics support the hypothesis that $Zn(C_6F_5)_2$ acts simultaneously as a *p*-dopant and a microstructure modifier. We propose that it is the combination of these synergistic effects that leads to OTFTs with maximum hole mobility value of 21.5 cm^2/Vs. The work not only highlights $Zn(C_6F_5)_2$ as a promising new additive for next generation optoelectronic devices, but also opens up new avenues in the search for high mobility organic semiconductors.

Main Text

The intentional introduction of impurities into traditional inorganic semiconductors, also known as doping, is an extremely valuable technology that underpins all modern inorganic semiconductor-based optoelectronics. Unfortunately, established doping approaches have proven largely inapplicable to emergent semiconductor material families such as organic semiconductors (OSCs).[1] [2] This is one of the reasons why the printed organic electronics market has been slow to realise.[3] For example, commercialisation of the organic thin-film transistor (OTFT) technology has been hindered by performance-related issues including poor operational stability, high contact resistance and modest charge carrier mobilities.[4] Although some of these issues could potentially be negated by controlled doping, just like in silicon electronics, exploiting similar approaches in

the field of OTFTs has proven challenging. This difficulty arises, firstly, from the low doping efficiency of established molecular dopants,[4] [5] [6] and secondly by the adverse effects associated with the introduction of the bulky dopant molecules into the host OSC.[1] [4] Therefore, the development of innovative doping methods, and/or materials, that circumvent these negative effects has become a priority in recent years.[3]

Over the past few years the Lewis acid tris(pentafluorophenyl)borane [$B(C_6F_5)_3$] was shown to offer an alternative approach to *p*-doping of OSCs.[7] [8] [9] [10] [11] [12] In several of these studies the benefits of incorporating $B(C_6F_5)_3$ were shown to be two-fold: *p*-doping whilst simultaneously altering the OSC layer's microstructure, with the latter effect drastically enhancing the semiconductor's crystallinity and charge carrier transport.[7] Although many questions still surround the fundamental mechanisms involved in $B(C_6F_5)_3$-induced *p*-doping, morphology-change and the relationship between the two effects, there is clear evidence that one or more synergistic mechanisms are responsible for improving the electrical performance of different electronic devices – not just OTFTs.[7] [9] For example, simple addition of $B(C_6F_5)_3$ has shown to improve the performance of organic light emitting diodes (OLEDs),[10] OTFT sensors,[13] batteries,[14] organic photovoltaics (OPVs) [8] [15] and perovskite photovoltaics.[11] [16] [17] In OTFTs, the simultaneous effects of *p*-doping and morphology-changes resulted to greatly increased charge carrier hole mobility (μ).[7] [9] Furthermore, solution-processed mobilities approaching single-crystal-like values have been achieved in small-molecule:polymer blend OTFTs doped with $B(C_6F_5)_3$.[7] The effects of $B(C_6F_5)_3$ on μ are more important now than ever, considering the recent spate of overestimated μ values that contaminated the literature.[18] [19] [20] [21] Given the broad applicability of $B(C_6F_5)_3$, we wondered whether other molecular Lewis acids with similar multifunctional properties, and influences on μ, exist.

Using the preliminary work on $B(C_6F_5)_3$ as the starting point,[7] we investigated the possibility of employing the zinc-based Lewis acid bis(pentafluorophenyl)zinc ($Zn(C_6F_5)_2$)[22] as a possible *p*-dopant and microstructure modifier in blend OTFTs composed of the small molecule 2,7-dioctyl[1]benzothieno [3,2-b][1]benzothiophene (C_8-BTBT) and the amorphous-like conjugated polymer indacenodithiophene-benzothiadiazole (C_{16}IDT-BT) (**Figure 1a**).[23] [24] [25] Remarkably, the addition of even a small amount of $Zn(C_6F_5)_2$ in the semiconductor blend results in OTFTs with maximum hole mobility of 21.5 cm^2/Vs. Analysis of the channel layer and transistor performance allows us to hypothesise that simultaneous *p*-doping and strong $Zn(C_6F_5)_2$-induced microstructural changes are synergistically responsible for the high mobility values achieved.

We selected $Zn(C_6F_5)_2$ for a number of reasons including, (i) it is a known Lewis acid, (ii) it is commercial available, and (iii) it has yet to be studied as an additive in OSCs. To begin with, we investigated the possible doping effect of $Zn(C_6F_5)_2$ using electron paramagnetic resonance (EPR) spectroscopy.[26] [27] EPR has been used successfully to study organic free radicals[28] and transition metals,[29] as well as detect Lewis acid-induced doping in semiconductors.[16] [11] [15] [17] For this experiment, we chose a blend consisting of C_8-BTBT and C_{16}IDT-BT because in our earlier work it showed the highest hole mobility values enabled upon doping with $B(C_6F_5)_3$.[7] **Figure 1b** shows the EPR results for a pristine (undoped) and a highly doped (30 mol% $Zn(C_6F_5)_2$) C_8-BTBT:C_{16}IDT-BT blend, where the desired concentration of $Zn(C_6F_5)_2$ was calculated as a molar percentage (mol%.) of the total combined molar mass of C_8-BTBT and C_{16}IDT-BT. Given that the samples were identical sizes and measured under the same conditions, the observed increase in signal can only be attributed to the addition of $Zn(C_6F_5)_2$. The pronounced EPR signal suggests that $Zn(C_6F_5)_2$ generates unpaired electrons in the blend, i.e. act as a *p*-dopant for the host

semiconductor. We note here that the high concentration of $Zn(C_6F_5)_2$ used (30 mol%) is due to its poor solubility in chloroform (**Figure S1**), which will be discussed further later.

Further supporting evidence of the possible *p*-doping action of $Zn(C_6F_5)_2$ comes from its blends with the wide band gap polymer semiconductor poly[bis(4-phenyl)(2,4,6-trimethylphenyl)amine] (PTAA) (**Figure 1c**). We have previously shown that adding $B(C_6F_5)_3$ in a PTAA solution induces a stark colour change, an effect attributed to the formation of adducts/charge transfer complexes between the Lewis acid and the host OSC.[7] [11] Unlike the $B(C_6F_5)_3$:PTAA blend, however, $Zn(C_6F_5)_2$:PTAA solutions prepared at room temperature showed no noticeable change in their appearance. Only upon heating the solution to 120 °C was it found to transform the initially clear $Zn(C_6F_5)_2$:PTAA solution to a light salmon-pink colour, which got darker upon storage at room temperature for three months (**Figure 1c**). These optical changes were further supported using UV-vis absorption spectroscopy (**Figure S2)**. To investigate whether integer charge transfer is responsible for the apparent *p*-doping effect,[24] [30] [31] the highest occupied molecular orbital (HOMO) and the lowest unoccupied molecular orbital (LUMO) position of $Zn(C_6F_5)_2$ was calculated using density functional theory (DFT). **Figure 1d** shows the energy level alignment between the various organic semiconductors and the calculated energetics for $Zn(C_6F_5)_2$. Evidently, the resulting energy diagram does not directly supports the integer charge transfer as a likely process, leaving the formation of Lewis-adducts as the most plausible mechanism.

Having shown that $Zn(C_6F_5)_2$ appears to function as a *p*-dopant, we began to explore its applicability in OTFTs. We added varying amounts of $Zn(C_6F_5)_2$ into C_8-BTBT:C_{16}IDT-BT blend solutions (0, 0.025, 0.25, 2.5 and 5 mol% $Zn(C_6F_5)_2$)), which were subsequently spin-coated and annealed at 120 °C in nitrogen atmosphere. Remarkably, the resultant C_8-BTBT:C_{16}IDT-

BT:$Zn(C_6F_5)_2$ transistors yield striking performance characteristics (**Figure 2a-b**). Addition of only 0.025 mol% $Zn(C_6F_5)_2$ increased μ_{SAT} from 1.9 cm^2/Vs to a maximum value of 21.5 cm^2/Vs (10× increase), as derived from the gradient of the $I_D^{0.5}$ *vs.* V_G plot in **Figure 2a**, measured at a drain potential (V_D) of -80 V for an OTFT with channel length (L) and width (W) of 100 and 1000 μm, respectively. To minimize any potential errors in the mobility calculations the geometric capacitance (C_i) of the CYTOP dielectric was determined for all transistors studied using capacitance-voltage measurements yielding a value of ≈1.7 nF/cm^2 (a representative plot is shown in **Figure S3**). The latter equates to a relative permittivity value for CYTOP (ε_{CYTOP}) between 2-2.1, in excellent agreement with the literature.

Despite the linearity of $\sqrt{I_D}$, it is still important to critically assess the reliability of μ_{SAT}, as overestimations can still occur when using the gradual channel approximation.[32] [21] To address this point, we examined the relationship between μ_{SAT} (calculated from the second derivative of I_D *vs.* V_G) and V_G (**Figure 2c**). Unlike several literature reports,[33] [21] [34] [32] [35] μ_{SAT} does not exhibit the often seen prominent roll-off with increasing V_G and it stabilises at around 20 cm^2/Vs (V_G = -80 V). At this bias the extracted value for μ_{SAT} is expected to be more reliable due to the suppressed contact resistance (R_C).[35] **Figure 2d** shows the statistical variations of μ_{SAT} and threshold voltage (V_T) for pristine and $Zn(C_6F_5)_2$-containing blend OTFTs, whilst **Figure S4** summarizes the variation of both μ_{SAT} and the linear mobility (μ_{LIN}) for 12 transistors fabricated simultaneously on the same substrate. In these plots, the μ_{SAT} values were derived both from fits to the linear part of the $\sqrt{I_D}$ *vs.* V_G curves as well as from the second derivative of the channel transconductance in the higher V_G range. Irrespective of the method employed, obtained μ_{SAT} values range from a minimum of ≈7 cm^2/Vs to a maximum of >21.5 cm^2/Vs (**Figure S4** and **S5**). Derived μ_{LIN} values are consistently lower with the maximum value just above 10 cm^2/Vs. We

attribute this to the significant R_C present even after addition of the $Zn(C_6F_5)_2$, as evident by the non-linear dependence of I_D at $V_D < 10$ V (**Figure 2b** and **S5**). Unfortunately, R_C measurements did not show any consistent differences between OTFTs incorporating different $Zn(C_6F_5)_2$ concentrations. A possible reason for this is the noticeable variability in the device performance (**Figure S4**) – a characteristic most likely attributed to the limited solubility of $Zn(C_6F_5)_2$ discussed earlier (**Figure S1**).

To understand the origin of the performance enhancement upon doping with $Zn(C_6F_5)_2$, we used a complementary range of materials characterisation techniques. **Figure 3a-d** show polarized optical microscopy (POM) and atomic force microscopy (AFM) images of the pristine (**Figure 3a-b**) and $Zn(C_6F_5)_2$-containing (0.025 mol%) (**Figure 3c-d**) blend layers. Both films appear highly crystalline, indicative of vertical phase separation between C_8-BTBT and C_{16}IDT-BT, which is typical for small-molecule/polymer blend systems, and further supported by the cross-sectional transmission electron microscopy (TEM) image shown in **Figure S6**.[36] [37] [23] [38] [39] Although the POM images do not show noticeable morphology differences between the pristine and $Zn(C_6F_5)_2$-containing layer, the AFM images reveal different molecular terracing behaviour which becomes more noticeable in the surface histograms of **Figure 3e**.[40] [41] The differences in terracing are also reflected in the root mean square (rms) surface roughness value, which decreases from 7.69 to 1.69 nm upon $Zn(C_6F_5)_2$ addition (**Figure 3e**). Detailed analysis of the distinguishable features in these histograms suggests strong commonalities but also stark differences. For instance, the height distribution for the pristine and $Zn(C_6F_5)_2$-containing blend layer extends up to ≈12 and ≈9.3 nm, respectively. Despite this difference, the overlapping parts of the histograms exhibit identical features (see arrows and corresponding heights), albeit with different intensities, indicative of similar surface texture but different size of the corresponding terraces, respectively.

Along with the fact that similar morphological influences have been reported previously for $B(C_6F_5)$ systems,[7] this data provides direct evidence of the strong impact of $Zn(C_6F_5)_2$ on the crystallization and growth of the vertically separated C_8-BTBT region (**Figure S6**) that forms the actual transistor channel studied in the top-gate device architecture used here.

To study the possible impact of $Zn(C_6F_5)_2$ addition on the microstructure of the blend layers in more detail, we performed grazing-incidence wide-angle X-ray scattering (GIWAXS) measurements. Indeed we find that introduction of $Zn(C_6F_5)_2$ induces minor changes in the C_8-BTBT in-plane peaks (including peak split and shift). **Figure 4** and **Table S1** show that, overall, although (11L) has remained the same (L=1, 2, 3…), the (02L) and (12L) *q*-spacings have decreased by ≈1%, from 1.604Å^{-1} and 1.945Å^{-1} in the pristine film, to 1.595Å^{-1} and 1.920Å^{-1} in the $Zn(C_6F_5)_2$-containing blend film. The in-plane anisotropic variation can be used to estimate the distortion in the *ab*-plane and the change in inter-molecular arrangement; adding $Zn(C_6F_5)_2$ is found to increase the lattice parameter along *b* [010] and, in order to keep constant (11L) spacing, decrease the lattice parameter along *a* [100], compressing the *a*-axis in-plane lattice by ≈1%. Because the C_8-BTBT herringbone motif –similar to rubrene[42]– prefers charge transport between π-stacking along the *a*-axis,[43] we conclude that such compression may shorten the π-π spacing and benefit charge transport (**Figure S8)**.[44] Similar minor changes introducing in-plane structure polymorphs have been previously reported.[45] Additionally, this subtle change may explain the lack of major morphological differences in the POM images (**Figure 3a**, **3c**), whilst supporting the observed differences in the AFM images (**Figure 3d**). Compared to C_8-BTBT, the C_{16}IDT-BT binder appears more disordered as previously noted,[46] and the presence of the dopant has no discernible influence on its ordering. We also found that the process of blending the C_8-BTBT with the C_{16}IDT-BT causes the former to undergo lattice shrinkage, with the in-plane peaks

showing improved edge-on, highly orientated scattering in the C_8-BTBT:C_{16}IDT-BT blend (**Figure 4a**). On the other hand, the (100) and (010) peaks associated with C_{16}IDT-BT, exhibit larger *q*-spacing in the C_8-BTBT:C_{16}IDT-BT blend, as compared to the neat polymer (**Figures 4b**, **S6**, **S7** and **Table S1**). Overall, the GIWAXS results shows that crystallization of C_8-BTBT is affected more by $Zn(C_6F_5)_2$ than the C_{16}IDT-BT. On the basis of these findings, we hypothesize that the new smaller C_8-BTBT lattice –together with the formation of larger molecular terraces– are most likely responsible for the consistently enhanced hole transport in $Zn(C_6F_5)_2$-containing blend OTFTs (**Figure 2**).

Although the evidence presented so far suggests that $Zn(C_6F_5)_2$-induced morphological-changes may play an important role in the mobility increase, it is also important to consider possible *p*-doping effects, as indicated by the EPR measurements in **Figure 1b** and the optical absorption measurements in **Figure S2**. The origin of Lewis acid-induced *p*-doping in organic semiconductors has been difficult to identify so far, primarily because the conditions for efficient integer charge transfer from the dopant to the host semiconductor(s) to occur, are not satisfied (**Figure 1d**).[9] An alternative doping model was therefore adopted,[47] which proposes the formation of a Lewis acid/base charge transfer complex (or adduct) that is characterized by lower HOMO and LUMO energy levels. It is the emergence of these new energy states that then facilitate the charge transfer process resulting in *p*-doping.[9] This mechanism was used to explain the results in a number of recent studies involving $B(C_6F_5)$,[8] [7] [16] [12] [10] where redistribution in the electron density in the semiconductor, caused by the interaction(s) between B in $B(C_6F_5)_3$) and nitrogen (N), lone pairs in the organic semiconductor, result in *p*-doping.[9] [13] [7] [11] [17]

Given that $B(C_6F_5)$ has been shown to act as a *p*-dopant, we took a further look into the OTFT data to evaluate whether $Zn(C_6F_5)_2$ incorporation can also induce noticeable *p*-doping in the

transistor channel. **Figure S5** presents the operating characteristics for the pristine and $Zn(C_6F_5)_2$-containing blend OTFTs with different dopant concentrations, and complements the data shown in **Figure 2a**. Unlike traditional molecular dopants,[24] [30] [31] [48] we do not observe the characteristic trend of the OTFT's off-current (I_{OFF}) increasing with increasing $Zn(C_6F_5)_2$ concentration. However, signs of *p*-doping come from the dependence of V_T on $Zn(C_6F_5)_2$ concentration (**Figure 2d**), which is found to shift from its initial value of -40 V (pristine blend OTFTs) to -20 V upon optimised $Zn(C_6F_5)_2$ concentrations (0.025 and 2.5 mol%), before it returns to a more negative value of -33 V at higher concentrations (5 mol%) (**Figure S5**). Furthermore, the μ_{SAT} *vs.* V_G plots in **Figure S5** can be used to gauge relative changes in R_C with increasing $Zn(C_6F_5)_2$ concentration, as indicated by the red arrows.[35] The steepening μ_{SAT} with increasing V_G observed in pristine blend OTFTs, along with a non-saturating output curve (**Figure S5a**), suggest the pristine devices comparatively suffer most from R_C. The most notable improvements in device behaviour occurs at 0.25 mol% $Zn(C_6F_5)_2$ (**Figure S5c**), where μ stabilises at higher V_G. The latter behaviour is also observed in 2.5 and 5 mol%.[35] Therefore, the μ_{SAT} *vs.* V_G plots suggest R_C gradually improves (reduces), in relation to the channel resistance (R_{CH}), with the addition of $Zn(C_6F_5)_2$, another characteristic often associated with doped OTFTs.[24]

Along with changes in transistor characteristics (**Figure S5**), the EPR data and UV-vis absorption spectroscopy results (**Figures 1b-c** and **S2**), we performed Kelvin probe (KP) measurements on the individual semiconductor layers before and after addition of $Zn(C_6F_5)_2$. **Figure S9** shows the change in the measured work function (ΔWF) for C_{16}IDT-BT and C_8-BTBT before and after the addition of $Zn(C_6F_5)_2$ at two concentrations (0.025 and 1 mol%). In the case of C_{16}IDT-BT, ΔWF appears to remain relatively constant with a small shift of ≈15 meV (at 1 mol%) towards lower energies. For C_8-BTBT, on the other hand, there is a much more substantial

shift by approximately 100 meV, under the same experimental conditions. Since material and sample preparation, as well as KP measurements, were performed entirely under inert atmosphere, the results can be considered as additional direct evidence for *p*-type doping. However, although the reason for the selective nature of the effect is not clear, it could simply be attributed to the slightly different energetics of the host materials (**Figure 1d**). We also note that a plausible reason for the absence of a 'stronger' *p*-doping effect at higher mol% may be the poor solubility of $Zn(C_6F_5)_2$ (**Figure S1**). On this basis, the data presented so far suggests $Zn(C_6F_5)_2$ interacts with both semiconductors, albeit in different ways. As we will discuss next, these interactions may also underpin the morphological changes observed in the AFM and GIWAXS data (**Figures 3** and **4**) and as such being –at least partially– responsible for the hole mobility improvement seen at optimal $Zn(C_6F_5)_2$ concentrations (**Figures 3**).[6] [8]

Further insight into the possible interactions between $Zn(C_6F_5)_2$ and the C_8-BTBT:C_{16}IDT-BT blend components were provided by density functional theory (DFT) calculations. A number of the DFT results are consistent with key points we have inferred from the experimental observations discussed above. Firstly, the calculated HOMO (-7.75 eV) and LUMO (-2.15 eV) energies for $Zn(C_6F_5)_2$ (**Figure 1d**) rule out the ground state integer charge transfer scenario. Secondly, we confirmed that $Zn(C_6F_5)_2$ interacts strongly with both C_8-BTBT and C_{16}IDT-BT by forming direct or stretched covalent bonds with various sites (such as C, N or S) on both semiconductors. We note that the complex between a pair of $Zn(C_6F_5)_2$ and C_8-BTBT molecules has the two moieties in a face-on configuration, which could be, in principle, seamlessly incorporated in the C_8-BTBT part of the blend, perhaps filling in voids and as such affecting the nucleation and growth dynamics of the phase-separated small-molecule (**Figure S6**) component

during solidification. However, a detailed study of the latter processes is beyond the scope of the present DFT calculations.

In previous investigations involving $B(C_6F_5)_3$, it was reported that its reaction with molecular oxygen resulted to a complex $[B(C_6F_5)_3\text{-}O_2]$ with significantly stronger electron accepting characteristics than $B(C_6F_5)_3$ alone.[49] We therefore performed similar calculations for $Zn(C_6F_5)_2$ and found that the formation of the complex with oxygen was indeed favourable, and that the formed $Zn(C_6F_5)_2\text{-}O_2$ complex had a significantly lower LUMO energy level of -4.78 eV (**Figure S10a**). Although device fabrication and characterization were performed in a nitrogen-filled glovebox, it is possible that the small amounts of oxygen still present either in the solvent(s), and/or inside the glovebox (≈1 ppm), could form oxidising complexes, such as the $Zn(C_6F_5)_2\text{-}O_2$, and lead to the apparent *p*-doping effect. To this end, we note that the HOMO levels of C_8-BTBT (-5.20 eV) and PTAA (-5.18 eV) are strikingly similar, and closer than C_{16}IDT-BT, to the calculated LUMO energy of the $Zn(C_6F_5)_2\text{-}O_2$ complex (-4.78 eV) shown in **Figure S10a**. This similarity, when considering the potential errors associated with the experimental measurements and theoretical calculations, could be the driving force for the apparent *p*-doping effect via a complex-mediated ground-state charge transfer process.

Figure S10b-c shows two additional molecular complexes that are likely to exhibit strong hybridization with C_{16}IDT-BT and C_8-BTBT. Similar to the case of the $Zn(C_6F_5)_2\text{-}O_2$ complex, the two adducts shown in **Figure S10b-c** exhibit significantly reduced HOMO energies and, in some cases, in the LUMO level as well. It is therefore plausible that formation of such complexes could alter the hole transport properties of the C_{16}IDT-BT:C_8-BTBT blend. One additional possibility is that the formation of the aforementioned molecular adducts/complexes may also cause the stark change in the layer's surface morphology (**Figure 3e**) similar to that reported for

$B(C_6F_5)_3$.[7] To this end, Han *et al*. recently reported that the addition of $B(C_6F_5)_3$ into a small-molecule:polymer blend, on one hand *p*-dopes one component, whilst influencing the crystallization properties of the other.[8] Our proposed mechanism is also in line with previously reported examples for integer charge transfer molecular dopants, whereby the transfer of charge subsequently influences the structural properties of the host semiconductor.[6] It is thus likely that similar mechanism(s) may also be at play with $Zn(C_6F_5)_2$, leading to the improved molecular terracing in C_8-BTBT:C_{16}IDT-BT layers (**Figure 3e**) and the formation of structural polymorphs (**Figure 4**).

In summary, we developed solution-processed blend OTFTs with a maximum hole mobility of over 20 cm^2/Vs using the previously unreported organic Lewis acid $Zn(C_6F_5)_2$. We showed that $Zn(C_6F_5)_2$ acts as a microstructure modifier that has a significant impact on the hole transport along the phase-separated semiconducting layers. The addition of minute amounts of $Zn(C_6F_5)_2$ into optimized C_8-BTBT:C_{16}IDT-BT blends results in a remarkable increase in hole mobility from a minimum value of ≈1.9 to a maximum of 21.5 cm^2/Vs; a value approaching the highest reported hole mobility for C_8-BTBT-based transistors,[30] and amongst the highest reported to date for solution-processed OTFTs.[21,55] Analysis of the materials and device characteristics indicates that $Zn(C_6F_5)_2$ has a dual functionality, possibly acting simultaneously as a microstructure modifier and a *p*-dopant. To this end, admixing of just 0.025 mol% of $Zn(C_6F_5)_2$ into the semiconducting blend enhances molecular terracing of C_8-BTBT, whilst encouraging the formation of polymorphs. The possibility that $Zn(C_6F_5)_2$ functions as *p*-dopant was investigated using EPR spectroscopy, UV-vis absorption spectroscopy, Kelvin Probe and field-effect transistor measurements, all of which suggest *p*-doping. To this end, the reduced solubility of $Zn(C_6F_5)_2$ appears to be a limiting factor, and most likely responsible for the apparent low doping efficiency.

Finally, DFT calculations predict a strong tendency for $Zn(C_6F_5)_2$ to hybridize with C_8-BTBT and C_{16}IDT-BT, as well as to form previously unreported oxidizing complexes with oxygen such as $Zn(C_6F_5)_2$-O_2, which could in turn be responsible for the apparent *p*-doping effect. The same intermolecular interactions could also underpin the different crystallisation kinetics seen in the doped blends, although further work would be required to elucidate the role(s) of such interactions. Overall, the present findings rekindle confidence in the OTFT's ability to reach high charge carrier mobilities, while highlighting the potential of molecular Lewis acids as effective multifunctional additives.

Experimental section

Organic semiconductor preparation: The C_8-BTBT:C_{16}IDT-BT blend formulation was prepared with 25% C_8-BTBT and 75% C_{16}IDT-BT (10 mg/ml) using a solvent blend of chlorobenzene and tetralin at 1:1 ratio, following previously reported procedures.[23, 24] The $Zn(C_6F_5)_2$ solution is prepared separately in chloroform at a concentration of 1 mg/ml, and stirred at 60°C for an hour, until a clear solution was formed. $Zn(C_6F_5)_2$ was then added to the C_8-BTBT:C_{16}IDT-BT blend solution at the desired concentrations and stirred overnight at room temperature. The PTAA solution was prepared in tetralin at a concentration of 20 mg/ml, C_8-BTBT was prepared in chlorobenzene at a concentration of 20 mg/ml, and C_{16}IDT-BT was prepared in chlorobenzene at a concentration of 5 mg/ml. The desired concentration of $Zn(C_6F_5)_2$ was calculated as a molar percentage (mol%) of the total combined molar mass of C_8-BTBT and C_{16}IDT-BT for the blend, and the total molar mass of either PTAA, C_8-BTBT or C_{16}IDT-BT for the other semiconductor solutions. For PTAA, C_8-BTBT and C_{16}IDT-BT, the $Zn(C_6F_5)_2$-treated solutions were heated to 120°C for 5 min once fully dissolved.

Thin-film transistor fabrication and measurements: Gold source/drain electrodes were thermally evaporated onto Borofloat glass that has been cleaned via ultrasonication in water/Decon90, acetone and 2-propanol (IPA). The gold electrodes were then functionalized with the self-assembling monolayer pentafluorothiophenol (PFBT), acting as a workfunction modifier, prior to semiconductor layer deposition. The C_8-BTBT:C_{16}IDT-BT:$Zn(C_6F_5)_2$ solution was stirred at 60°C for 30 minutes before depositing via spin-coating in two steps: 1) 500 rpm for 10 seconds and 2) 1500 rpm for 30 s. After spin-coating, the C_8-BTBT:C_{16}IDT-BT:$Zn(C_6F_5)_2$ blend thin-films were immediately placed on a hotplate at 120 °C, where the latter annealing/heating step is believed to be critical to successful $Zn(C_6F_5)_2$ processing. A layer of Cytop dielectric was then deposited on top of the semiconductor, followed by the deposition of a 50 nm-thick aluminium gate electrode via vacuum sublimation in high vacuum. Finally, the current-voltage characteristics of the devices were recorder using a Keysight B2912A Precision Source/Measure Unit.

Capacitance-frequency measurements: A metal-insulator-metal (MIM) structure, consisting of an aluminium top electrode and an ITO bottom-electrode, was used to measure the capacitance-voltage-frequency (C-V-*f*) characteristics of Cytop dielectric in nitrogen atmosphere. All measurements we performed using a Solartron SI 1260 impedance analyser in the frequency range 10-100 kHz employing a DC level of 0 V and an AC level of 0.02 V. Each MIM device had an active area of 0.1 cm^2.

DFT calculations: DFT calculations were performed using the code NWCHEM[50] and the B3LYP [51] [52] exchange-correlation functional. The relaxation of structure was typically performed with the 6-31G* or 6-311G* Gaussian basis sets, and van der Waals interactions were included with the so-called DFT-D3 method. [53] The calculations of HOMO and LUMO energy values were also performed with the more complete 6-311G* or 6-311+G* bases, whenever that was feasible.

Polarised optical microscopy: A Zeiss AX10 polarised optical microscopy was used to record the optical microscope images of the solid films.

Atomic force microscopy: AFM measurements were carried out in tapping mode using an Agilent 5500, with a scanning speed of 0.2 lines/s. Gwyddion software was used for further data processing and statistical analysis.

Grazing-incident wide-angle X-ray scattering (GIWAXS): GIWAXS measurements were carried out at the 11-BM Complex Materials Scattering (CMS) beamline of the National Synchrotron Light Source II (NSLS-II), Brookhaven National Laboratory. X-rays with wavelength 0.0918 nm were shone onto the thin-film samples at the incident angle of 0.10°. An in-vacuum CCD (Photonic Science) detector was tilted at ≈19° from the incident X-ray beam direction and located 227 mm away from the samples, which were calibrated by silver behenate. The measurements were performed in vacuum with the exposure time of 100 s to minimize the air scattering. To gain sharp scattering peaks with higher resolution, especially at high Q, most of the films were wiped out and only a slice (≈5 mm in x-ray direction) was left for GIWAXS. The data was analyzed by SciAnalysis, where plots of intensity versus q were integrated in various sections, including in the cake slice of 30° along Q_z, in the rectangular area along Q_r, and in the overall pattern.

Electron paramagnetic resonance (EPR): All EPR spectra were recorded using x-band continuous wave Bruker EMX PLUS spectrometer (BrukerBioSpin, Rheinstetten, Germany) equipped with standard resonator for high sensitivity CW-EPR and operating at (9.384688) GHz. The low temperature spectra were measured using a liquid helium setup with 25 dB microwave attenuation with 5 GHz modulation amplitude and 100 kHz modulation frequency. In addition to carrying out the measurements under exactly the same operational conditions and temperatures (5 K), careful

attention was paid to sample preparation to ensure that identical sample quantities were being compared, i.e. the $Zn(C_6F_5)_2$ content was the only difference between samples.

Transmission Electron Microscopy (TEM): Cross-sectional TEM imaging of the samples was performed using a Titan 80-300 ST from Thermo-Fisher Scientific equipped with a spherical aberration corrector for the condenser lens and an energy-filter GIF-Quantum 966 from Gatan Inc. Analysis of the samples was performed using an operating voltage of 300 kV. Morphology and thickness of each layer in the stacks were investigated using the bright-field TEM (BF-TEM) mode of the instrument. The elemental distribution was determined using the energy-filter TEM mode (GIF-Quantum). The so-called 3-window method was utilized in order to generate the elemental maps the energy-loss edges of each element of interest.

Acknowledgements

T.D.A., A.F.P. and H.F. acknowledge the King Abdullah University of Science and Technology (KAUST) for financial support. R. Li used CMS beamline of the National Synchrotron Light Source II, a U.S. Department of Energy (DOE) office of Science User Facility operated for the DOE Office of Science by Brookhaven National Laboratory under contract No. DE-SC0012704. L. T. acknowledges support for the computational time granted from GRNET in the National HPC facility – ARIS – under project STEM.

References

[1] B. Lüssem, M. Riede, K. Leo, physica status solidi (a) 2013, 210, 9.

[2] K. Walzer, B. Maennig, M. Pfeiffer, K. Leo, Chemical Reviews 2007, 107, 1233.

[3] Y. Xu, H. Sun, A. Liu, H.-H. Zhu, W. Li, Y.-F. Lin, Y.-Y. Noh, Advanced Materials 2018, 30, 1801830.

[4] B. Lüssem, C.-M. Keum, D. Kasemann, B. Naab, Z. Bao, K. Leo, Chemical Reviews 2016.

[5] I. Salzmann, G. Heimel, M. Oehzelt, S. Winkler, N. Koch, Accounts Chem. Res. 2016, 49, 370.

[6] I. E. Jacobs, A. J. Moulé, Adv. Mater. 2017, 29, 1703063.

[7] J. Panidi, A. F. Paterson, D. Khim, Z. Fei, Y. Han, L. Tsetseris, G. Vourlias, P. A. Patsalas, M. Heeney, T. D. Anthopoulos, Advanced Science 2018, 5, 1700290.

[8] Y. Han, C. Jianya, Z. Ke, T. Yabing, M. Xiangyi, X. Xianbin, M. Wei, Advanced Energy Materials 2018, 0, 1703672.

[9] Y. Han, G. Barnes, Y.-H. Lin, J. Martin, M. Al-Hashimi, S. Y. AlQaradawi, T. D. Anthopoulos, M. Heeney, Chemistry of Materials 2016, 28, 8016.

[10] P. Zalar, Z. B. Henson, G. C. Welch, G. C. Bazan, T. Q. Nguyen, Angew. Chem.-Int. Edit. 2012, 51, 7495.

[11] J. Luo, J. Xia, H. Yang, L. Chen, Z. Wan, F. Han, H. A. Malik, X. Zhu, C. Jia, Energy & Environmental Science 2018.

[12] Z. Peter, K. Martijn, H. Z. B., W. Cristiano, Z. Yuan, S. Alexander, B. G. C., N. Thuc-Quyen, Advanced Materials 2014, 26, 724.

[13] W. G. Huang, K. Besar, R. LeCover, A. M. Rule, P. N. Breysse, H. E. Katz, Journal of the American Chemical Society 2012, 134, 14650.

[14] Y. M. Lee, Y. G. Lee, Y. M. Kang, K. Y. Cho, Electrochem. Solid State Lett. 2010, 13, A55.

[15] P. Patrick, A. Malavika, K. Lisa, S. Robert, K. Felix, B. Jan, J. Silvia, N. Dieter, Advanced Electronic Materials 2016, 2, 1600204.

[16] C. W. Koh, J. H. Heo, M. A. Uddin, Y. W. Kwon, D. H. Choi, S. H. Im, H. Y. Woo, ACS Appl. Mater. Interfaces 2017, 9, 43846.

[17] T. L. Ye, J. H. Wang, W. B. Chen, Y. L. Yang, D. Q. He, ACS Appl. Mater. Interfaces 2017, 9, 17923.

[18] A. F. Paterson, S. Singh, K. J. Fallon, T. Hodsden, Y. Han, B. C. Schroeder, H. Bronstein, M. Heeney, I. McCulloch, T. D. Anthopoulos, Advanced Materials, 0, 1801079.

[19] Y. Xu, H. Sun, A. Liu, H. Zhu, B. Li, T. Minari, F. Balestra, G. Ghibaudo, Y.-Y. Noh, Advanced Functional Materials 2018, 28, 1803907.

[20] H. Li, N. Tessler, J.-L. Brédas, Advanced Functional Materials 2018, 28, 1803096.

[21] H. H. Choi, K. Cho, C. D. Frisbie, H. Sirringhaus, V. Podzorov, Nature Materials 2017, 17, 2.

[22] A. J. Mountford, S. J. Lancaster, S. J. Coles, P. N. Horton, D. L. Hughes, M. B. Hursthouse, M. E. Light, Organometallics 2006, 25, 3837.

[23] A. F. Paterson, N. D. Treat, W. Zhang, Z. Fei, G. Wyatt-Moon, H. Faber, G. Vourlias, P. A. Patsalas, O. Solomeshch, N. Tessler, M. Heeney, T. D. Anthopoulos, Advanced Materials 2016, 28, 7791.

[24] A. F. Paterson, Y.-H. Lin, A. D. Mottram, Z. Fei, M. R. Niazi, A. R. Kirmani, A. Amassian, O. Solomeshch, N. Tessler, M. Heeney, T. D. Anthopoulos, Advanced Electronic Materials, 1700464.

[25] A. F. Paterson, A. D. Mottram, H. Faber, M. R. Niazi, Z. Fei, M. Heeney, T. D. Anthopoulos, Advanced Electronic Materials, 0, 1800723.

[26] D. Kiefer, A. Giovannitti, H. Sun, T. Biskup, A. Hofmann, M. Koopmans, C. Cendra, S. Weber, L. J. Anton Koster, E. Olsson, J. Rivnay, S. Fabiano, I. McCulloch, C. Müller, ACS Energy Letters 2018, 3, 278.

[27] Y. Han, Z. Fei, Y.-H. Lin, J. Martin, F. Tuna, T. D. Anthopoulos, M. Heeney, npj Flexible Electronics 2018, 2, 11.

[28] S. M. Mattar, A. H. Emwas, L. A. Calhoun, Journal of Physical Chemistry A 2004, 108, 11545; S. M. Mattar, A. H. Emwas, A. D. Stephens, Chemical Physics Letters 2002, 363, 152; S. M. Mattar, A. D. Stephens, A. H. Emwas, Chemical Physics Letters 2002, 352, 39.

[29] A.-H. M. Emwas, Z. A. Al-Talla, X. Guo, S. Al-Ghamdi, H. T. Al-Masri, Magnetic Resonance in Chemistry 2013, 51, 255.

[30] E. Lim, B.-J. Jung, M. Chikamatsu, R. Azumi, Y. Yoshida, K. Yase, L.-M. Do, H.-K. Shim, Journal of Materials Chemistry 2007, 17, 1416.

[31] Y. Abe, T. Hasegawa, Y. Takahashi, T. Yamada, Y. Tokura, Applied Physics Letters 2005, 87, 153506.

[32] T. Uemura, C. Rolin, T.-H. Ke, P. Fesenko, J. Genoe, P. Heremans, J. Takeya, Advanced Materials 2016, 28, 151.

[33] I. McCulloch, A. Salleo, M. Chabinyc, Science 2016, 352, 1521.

[34] E. G. Bittle, J. I. Basham, T. N. Jackson, O. D. Jurchescu, D. J. Gundlach, Nat Commun 2016, 7.

[35] C. Liu, G. Li, R. Di Pietro, J. Huang, Y.-Y. Noh, X. Liu, T. Minari, Phys. Rev. Appl. 2017, 8, 034020.

[36] R. Hamilton, J. Smith, S. Ogier, M. Heeney, J. E. Anthony, I. McCulloch, J. Veres, D. D. C. Bradley, T. D. Anthopoulos, Advanced Materials 2009, 21, 1166.

[37] J. Smith, W. M. Zhang, R. Sougrat, K. Zhao, R. P. Li, D. K. Cha, A. Amassian, M. Heeney, I. McCulloch, T. D. Anthopoulos, Advanced Materials 2012, 24, 2441.

[38] M. R. Niazi, R. Li, E. Qiang Li, A. R. Kirmani, M. Abdelsamie, Q. Wang, W. Pan, M. M. Payne, J. E. Anthony, D.-M. Smilgies, S. T. Thoroddsen, E. P. Giannelis, A. Amassian, Nature communications 2015, 6, 8598.

[39] S. Hunter, T. D. Anthopoulos, Advanced Materials 2013, 25, 4320.

[40] H. Minemawari, T. Yamada, H. Matsui, J. Tsutsumi, S. Haas, R. Chiba, R. Kumai, T. Hasegawa, Nature 2011, 475, 364.

[41] T. Izawa, E. Miyazaki, K. Takimiya, Advanced Materials 2008, 20, 3388.

[42] V. C. Sundar, J. Zaumseil, V. Podzorov, E. Menard, R. L. Willett, T. Someya, M. E. Gershenson, J. A. Rogers, Science 2004, 303, 1644.

[43] L. Jiang, J. Liu, X. Lu, L. Fu, Y. Shi, J. Zhang, X. Zhang, H. Geng, Y. Hu, H. Dong, L. Jiang, J. Yu, W. Hu, Journal of Materials Chemistry C 2018, 6, 2419.

[44] S. Riera-Galindo, A. Tamayo, M. Mas-Torrent, ACS Omega 2018, 3, 2329.

[45] M. L. Francisco, Y. Hongping, G. Xiaodan, K. Yeongin, T. M. F., B. Zhenan, Advanced Functional Materials 2017, 27, 1605503.

[46] X. Zhang, H. Bronstein, A. J. Kronemeijer, J. Smith, Y. Kim, R. J. Kline, L. J. Richter, T. D. Anthopoulos, H. Sirringhaus, K. Song, M. Heeney, W. Zhang, I. McCulloch, D. M. DeLongchamp, Nature communications 2013, 4, 2238.

[47] H. Méndez, G. Heimel, A. Opitz, K. Sauer, P. Barkowski, M. Oehzelt, J. Soeda, T. Okamoto, J. Takeya, J.-B. Arlin, J.-Y. Balandier, Y. Geerts, N. Koch, I. Salzmann, Angewandte Chemie International Edition 2013, 52, 7751.

[48] J. H. Kim, S. W. Yun, B.-K. An, Y. D. Han, S.-J. Yoon, J. Joo, S. Y. Park, Advanced Materials 2013, 25, 719.

[49] J. T. Henthorn, T. Agapie, Angewandte Chemie International Edition 2014, 53, 12893.

[50] M. Valiev, E. J. Bylaska, N. Govind, K. Kowalski, T. P. Straatsma, H. J. J. V. Dam, D. Wang, J. Nieplocha, E. Aprá, T. L. Windus, W. A. deJong, Computer Physics Communications 2010, 181, 1477.

[51] A. D. Becke, The Journal of Chemical Physics 1993, 98, 5648.

[52] P. J. Stephens, F. J. Devlin, C. F. Chabalowski, M. J. Frisch, The Journal of Physical Chemistry 1994, 98, 11623.

[53] S. Grimme, J. Antony, S. Ehrlich, H. Krieg, The Journal of Chemical Physics 2010, 132, 154104.

Figures

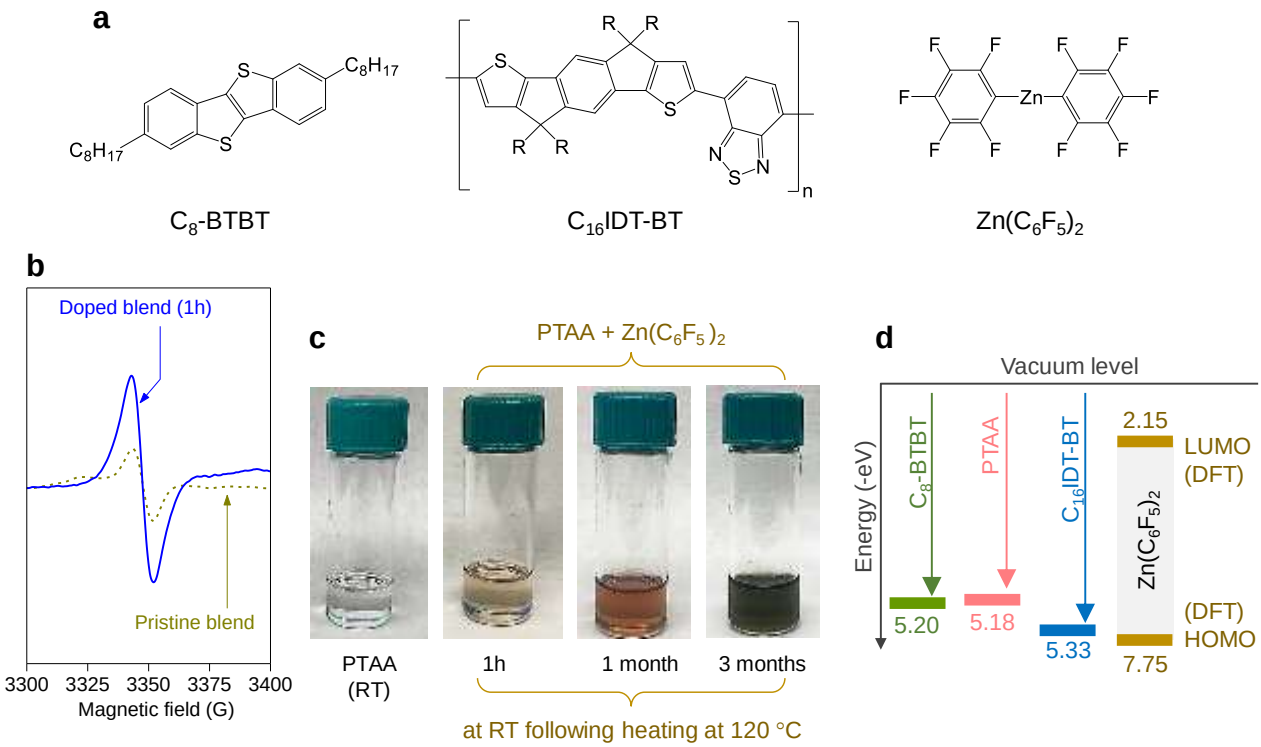

Figure 1. (a) Chemical structures of 2,7-dioctyl[1]benzothieno[3,2-*b*][1]benzothiophene (C_8-BTBT) and indacenodithiophene-benzothiadiazole (C_{16}IDT-BT) used in the C_8-BTBT:C_{16}IDT-BT blend, that acted as a host organic semiconducting system in thin-film transistors. Chemical structure of the zinc-based Lewis acid, bis(pentafluorophenyl)zinc ($Zn(C_6F_5)_2$) used to dramatically increase the mobility of C_8-BTBT:C_{16}IDT-BT blend. (b) Electron paramagnetic resonance spectroscopy signal responses for pristine C_8-BTBT:C_{16}IDT-BT and highly doped C_8-BTBT:C_{16}IDT-BT:$Zn(C_6F_5)_2$ (30%) blend. (c) Images showing the colour change of PTAA solution upon admixing $Zn(C_6F_5)_2$ and heating at 120 °C, as well as additional colour change over time, indicative of adduct formation. (d) Energy level diagram for the various materials employed. The DFT calculations for $Zn(C_6F_5)_2$ were based on the 6-311+G* basis. The HOMO energies for C_8-BTBT and C_{16}IDT-BT were measured experimentally using the photoelectron spectroscopy in air (PESA) technique.

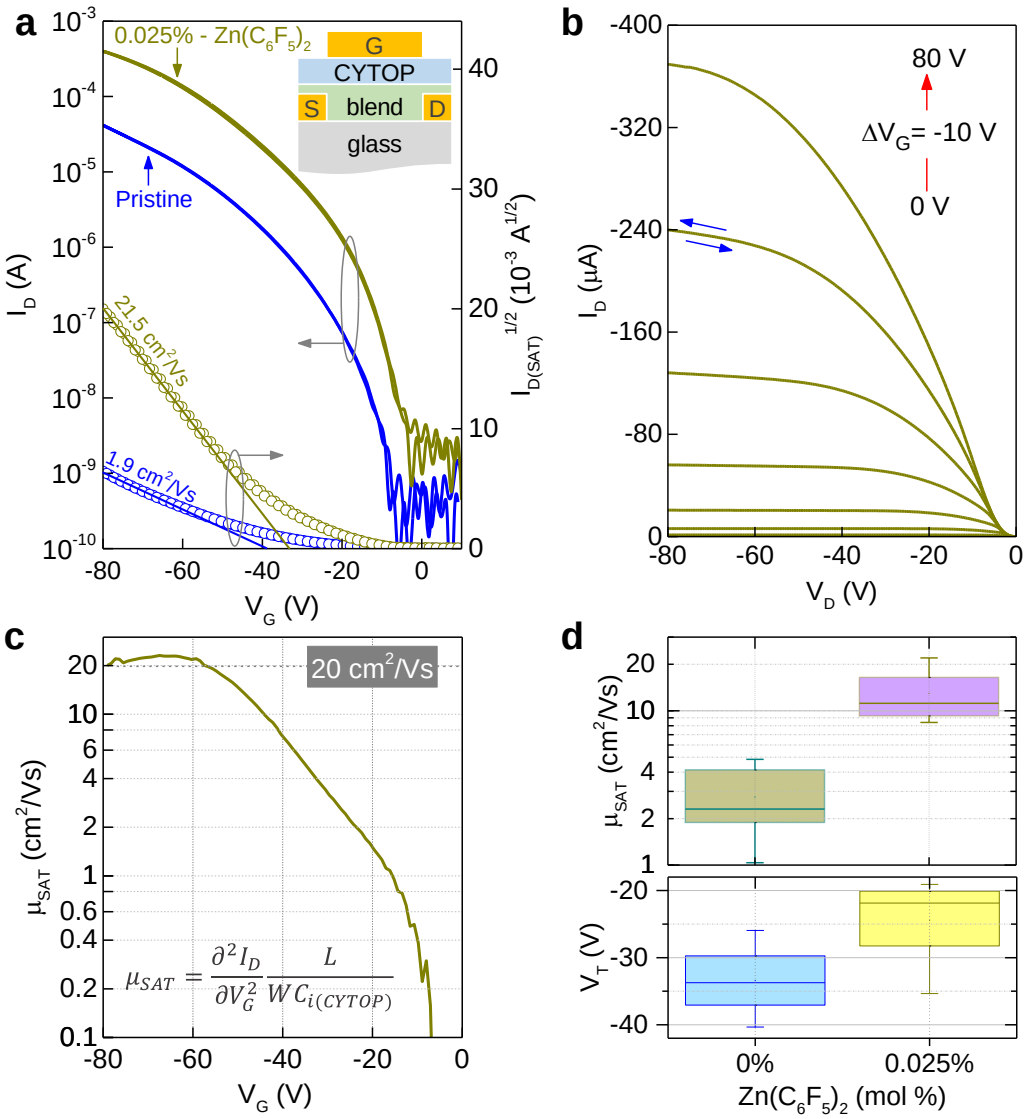

Figure 2. (a) Transfer curves for pristine (mol% $Zn(C_6F_5)_2$) and best-performing (0.025 mol% $Zn(C_6F_5)_2$) C_8-BTBT:C_{16}IDT-BT devices, measured at V_D = -80 V. (b) Output curve for the best-performing 0.025% $Zn(C_6F_5)_2$ C_8-BTBT:C_{16}IDT-BT device. Inset in (a) shows the transistor architecture used throughout this work. The devices shown have a channel length of 100 µm and width of 1000 µm, and geometric capacitance is 1.7 nF cm^{-2} (see Figure S3). (c) Plot of the second derivative μ_{SAT} vs. V_G for the best performing 0.025% $Zn(C_6F_5)_2$ C_8-BTBT:C_{16}IDT-BT device shown in (a) and (b). (d) Box-and-whisker plots showing saturation mobility and threshold voltage statistics and variability for pristine devices (0 mol% $Zn(C_6F_5)_2$) compared to best-performing devices (0.025 mol% $Zn(C_6F_5)_2$). The statistics in (d) are taken from 12 devices.

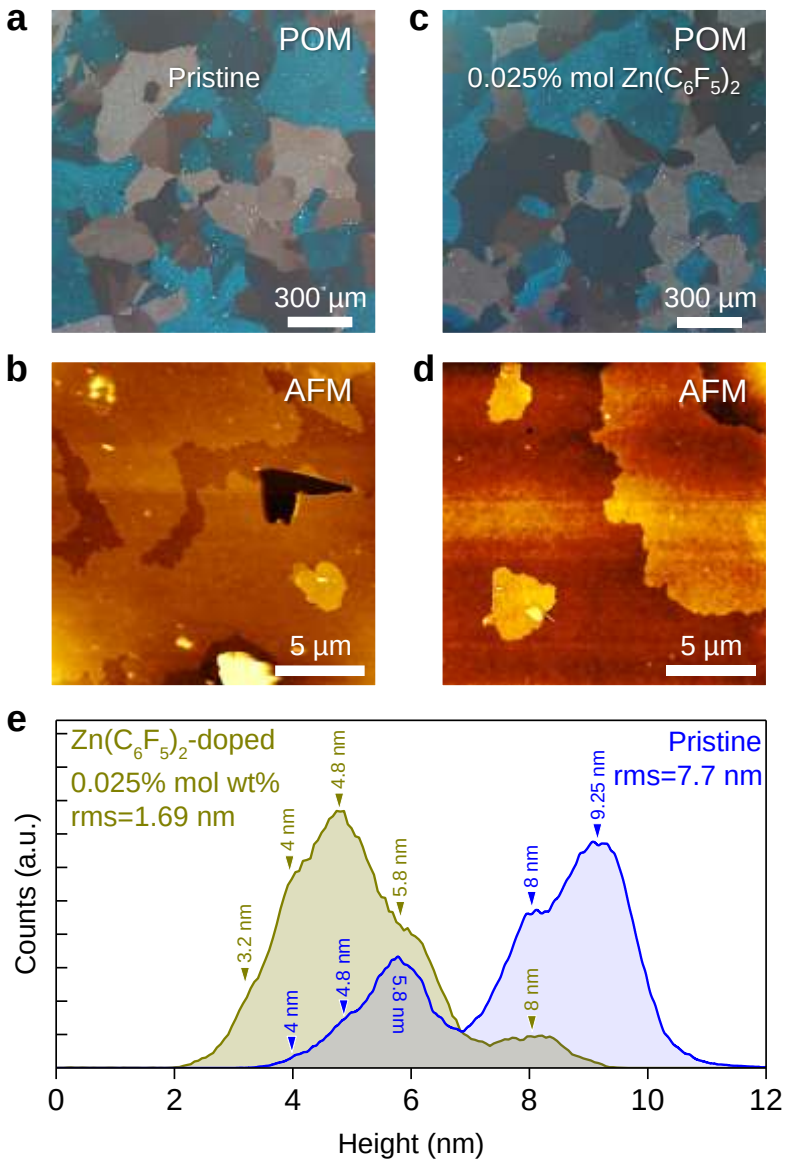

Figure 3. Morphology studies to investigate the impact of $Zn(C_6F_5)_2$ on the C_8-BTBT:C_{16}IDT-BT blend microstructure, at the best performing concentration of 0.025 mol% $Zn(C_6F_5)_2$. (a),(c) and (b),(d) are the polarised optical microscope and atomic force microscopy images of the pristine and best performing OSC layers, respectively. (e) Histogram showing height distribution for pristine blend and best performing $Zn(C_6F_5)_2$ blend.

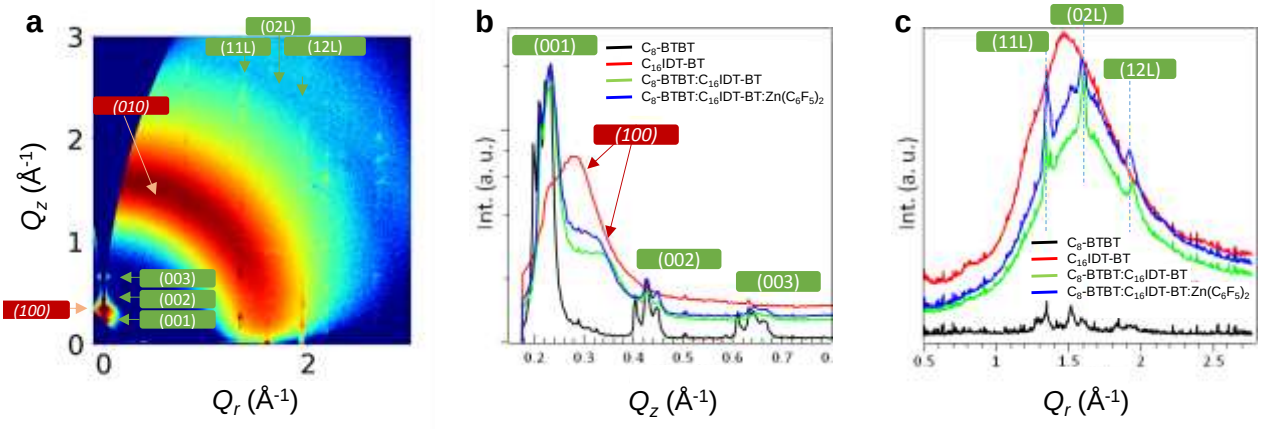

Figure 4. (a) Typical GIWAXS pattern with indexing peaks for C_8-BTBT (green) and C_{16}IDT-BT (pink). (b) and (c) are plots of intensity vs. q_z and q_r, representing the out-of-plane and in-plane peaks, respectively. The dashed lines in (c) are for eye guidance.

Supporting Information

Addition of the Lewis Acid $Zn(C_6F_5)_2$ Enables Organic Transistors with a Maximum Hole Mobility in Excess of 20 cm^2/Vs

Alexandra F. Paterson, Leonidas Tsetseris, Ruipeng Li, Aniruddha Basu, Hendrik Faber, Abdul-Hamid Emwas, Julianna Panidi, Zhuping Fei, Muhammad R. Niazi, Dalaver H. Anjum, Martin Heeney, Thomas D. Anthopoulos**

Figure S1. Image showing the solubility of $Zn(C_6F_5)_2$ in chloroform. Photographs of: (a) the chloroform solvent used, and (b) the $Zn(C_6F_5)_2$ in chloroform solution. As shown in (b), the $Zn(C_6F_5)_2$ does not dissolve fully, resulting in the appearance of a cloudy (saturated) solution.

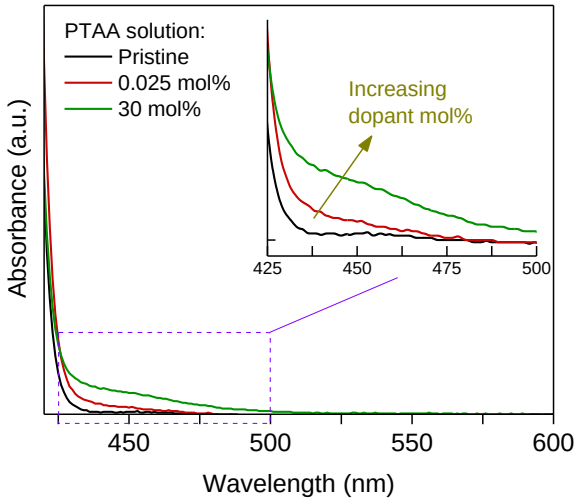

Figure S2. UV-vis absorption spectroscopy in PTAA with 0, 0.025 and 30 mol% of $Zn(C_6F_5)_2$, where the appearance of an additional absorption shoulder between 420 and 520 nm is clearly visible. The intensity of this absorption feature depends on the $Zn(C_6F_5)_2$ concentration but saturates quickly at relatively low concentrations, most likely due to the saturated solution (see **Fig. S1b**).

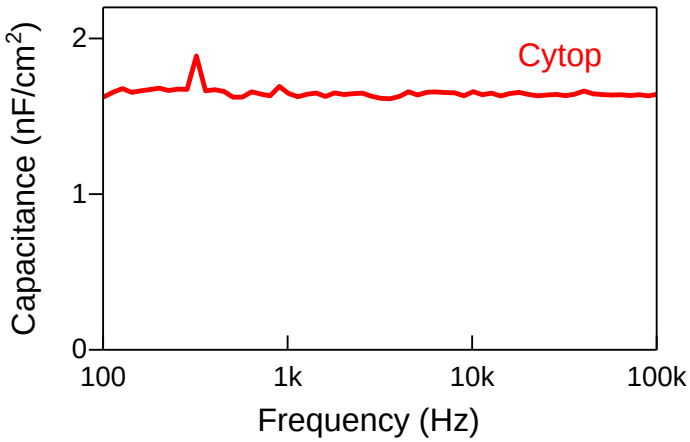

Figure S3. Capacitance-frequency measurement on the Cytop layer used to make the C_8-BTBT:C_{16}IDT-BT and C_8-BTBT:C_{16}IDT-BT:Zn(C_6F_5)$_2$ OTFTs, to determine the capacitance per area value used to calculate the mobility.

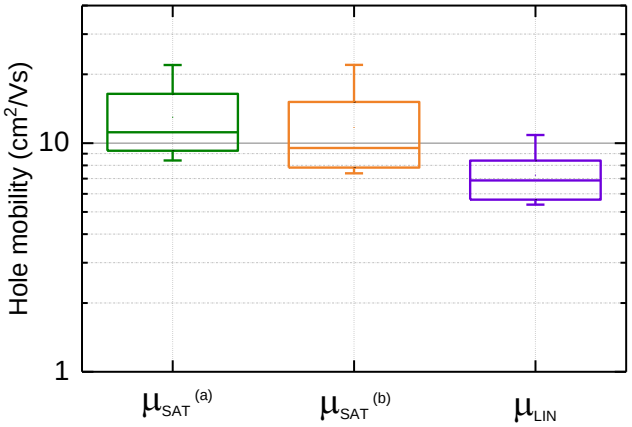

Figure S4. Box-and-whisker plot showing linear and saturation mobility statistics and variability for 0.025% Zn(C_6F_5)$_2$ devices, where (a) is the saturation mobility taken from $\sqrt{I_{D\_SAT}}$ and (b) is the saturation mobility taken from the highest V_G on plot of μ_{SAT}. The mobility statistics are taken from 12 devices.

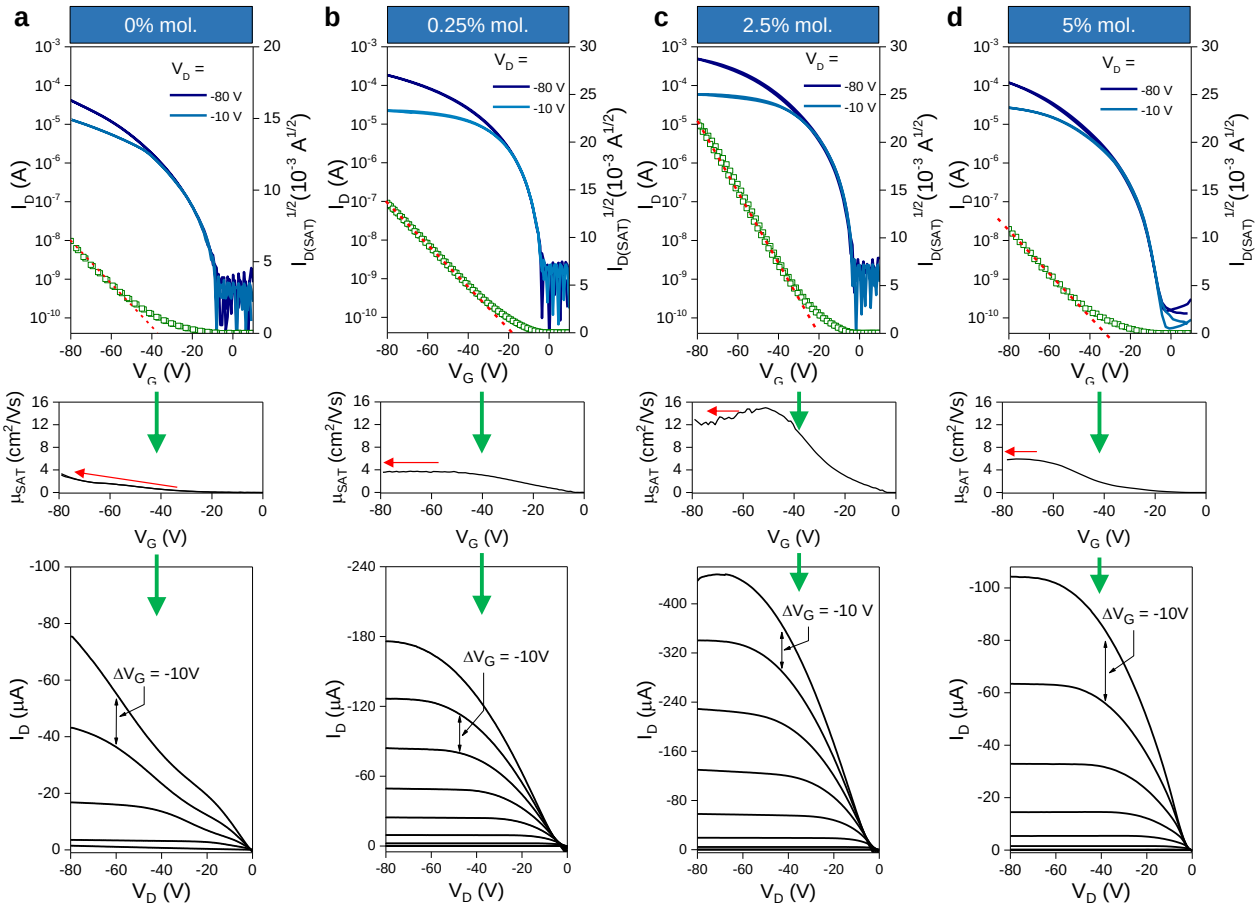

Figure S5. C_8-BTBT:C_{16}IDT-BT transistors with a range of $Zn(C_6F_5)_2$ concentrations (0, 0.25, 2.5 and 5 mol%). The devices have 80 µm channel length (L), 1000 µm channel width (W) and based on Cytop dielectric. All measurements were obtained with V_D = -10 V, and V_D = -80 V. For each concentration, transfer curves, output curves and corresponding plots of bias-dependent mobility are shown. The red arrows indicate features in the bias-dependent mobilities that can be used to extract information about the contact resistance.

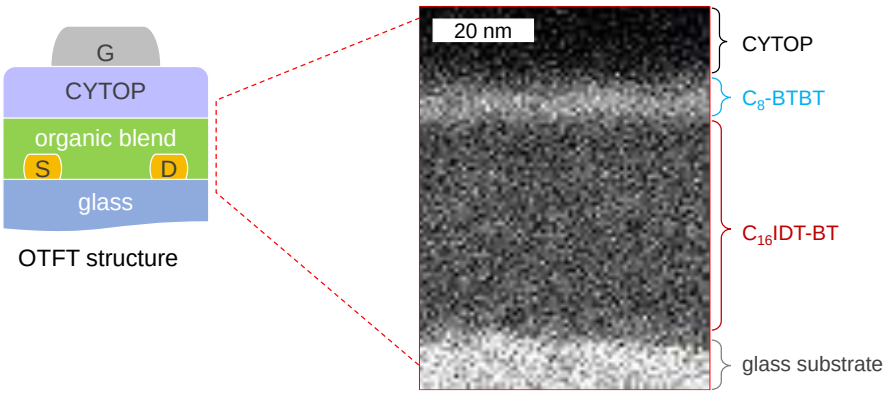

Figure S6. Transmission electron microscopy (TEM) image showing the spontaneous vertical phase separation between the C_8-BTBT and C_{16}IDT-BT in a pristine C_8-BTBT:C_{16}IDT-BT blend. The phase separated film consists of a highly crystalline C_8-BTBT on top of a layer of C_{16}IDT-BT after solution-processing (spin-coating).

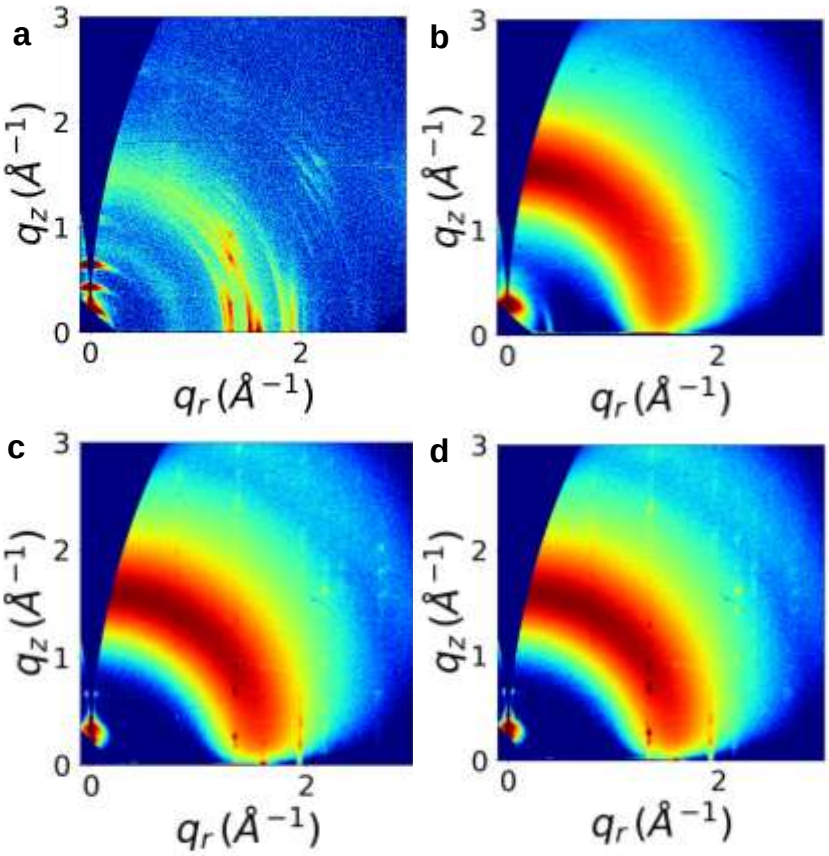

Figure S7. GIWAXS patterns of; (a) the neat C_8-BTBT small-molecule, (b) neat C_{16}IDT-BT polymer, (c) C_8-BTBT:C_{16}IDT-BT blend, and (d) C_8-BTBT:C_{16}IDT-BT:$Zn(C_6F_5)_2$ blend.

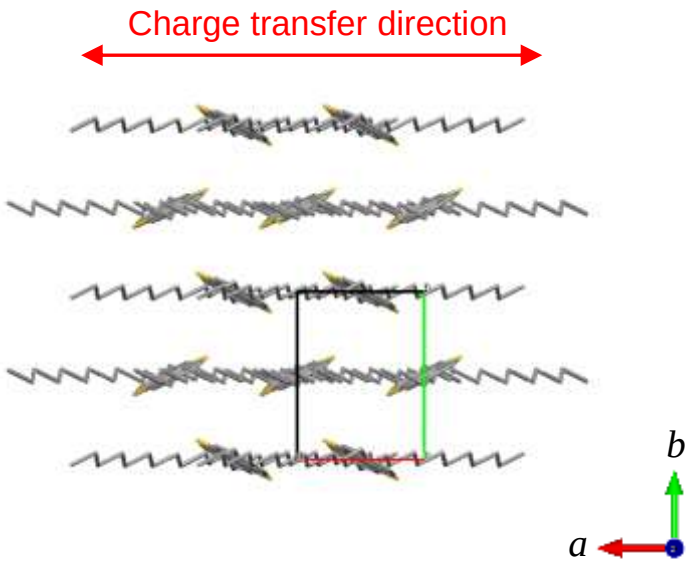

Figure S8. Schematic showing C_8-BTBT molecular stacking in the *ab*-plane. The preferred charge transfer direction is also shown to be along the a-axis.

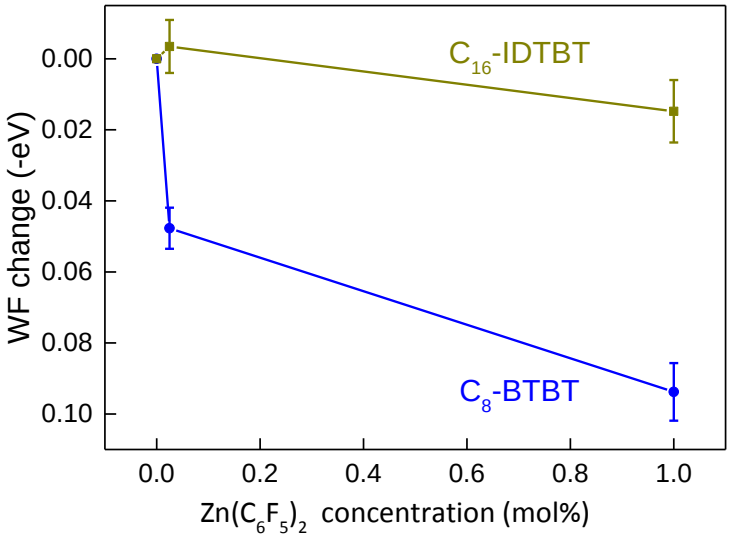

Figure S9. Kelvin Probe measurements showing changes in the C_8-BTBT and C_{16}IDT-BT work functions upon the addition of three different concentrations of $Zn(C_6F_5)_2$.

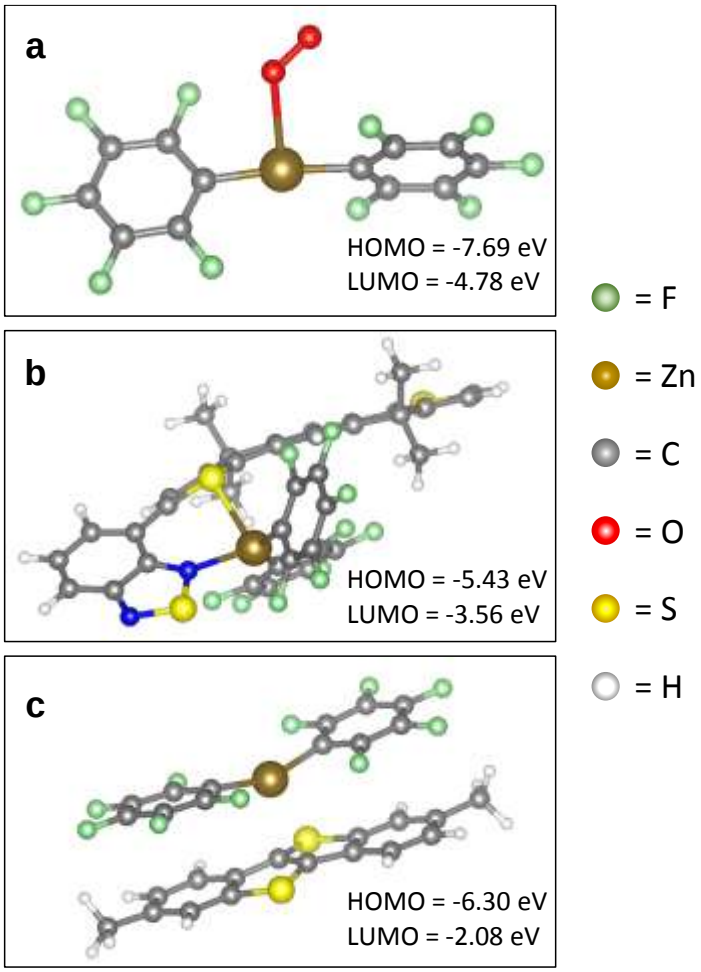

Figure S10. Density functional theory (DFT) calculations. (a) $Zn(C_6F_5)_2$-O_2 complex (spin-triplet state with E_{HOMO} = -7.69 eV and E_{LUMO} = -4.78 eV) with a binding energy of 0.22 eV with respect to isolated $Zn(C_6F_5)_2$ and O_2 molecules (6-311G* basis). (b) Adduct complex of the IDT-BT monomer and a $Zn(C_6F_5)_2$ molecule (E_{HOMO} = -5.43 eV and E_{LUMO} = -3.56 eV) with a binding energy of 1.77 eV with respect to isolated $Zn(C_6F_5)_2$ and IDT-BT molecules (6-311G* basis). The Zn-N and Zn-S bond lengths are equal to 2.14 Å and 2.63 Å, respectively. The E_{HOMO} and E_{LUMO} values were calculated with an 6-311+G* basis for C and F, 6-31G* for Zn. (c) Adduct complex of a BTBT and a $Zn(C_6F_5)_2$ molecule (E_{HOMO} = -6.30 eV and E_{LUMO} = -2.08 eV) with a binding energy of 1.53 eV with respect to isolated $Zn(C_6F_5)_2$ and BTBT molecules (6-311G* basis). The distance between the Zn and the underlying C atoms of BTBT is 2.71 Å (could be described also as two stretched Zn-C bonds).

Table S1. A summary of q- or d-spacing in C_8-BTBT, C_{16}IDT-BT, C_8-BTBT:C_{16}IDT-BT and C_8-BTBT:C_{16}IDT-BT:$Zn(C_6F_5)_2$ thin-film samples. The *q*-spacing units are nm^{-1} and *d*-spacing units are nm.

Semiconductor	**C_8-BTBT**				**C_{16}IDT-BT**	
	***q*(001)**	***q*(20L)**	***q*(02L)**	***q*(02L)**	***d*(100)**	***d*(010)**
C_8-BTBT	0.23	1.345	1.60	1.93	-	-
C_{16}IDT-BT	-	-	-	-	2.27	0.403
C_8-BTBT:C_{16}IDT-BT	0.2325	1.35/1.376	1.604	1.945	1.95	0.395
C_8-BTBT:C_{16}IDT-BT: $Zn(C_6F_5)_2$ (0.025 mol%)	0.233	1.358	1.595	1.920	2.02	0.393